

TRANSMISSION AND REFLECTION OF LIGHT IN PTFE FOR DARK MATTER RESEARCH

1 Summary

Polytetrafluoroethylene (PTFE), often known by its brand name Teflon, is extensively used in rare event searches, including Dark Matter (DM) experiments. Indeed, to efficiently collect the Vacuum Ultra-Violet scintillation light (~ 178 nm) emitted by Liquid Xenon (LXe) detectors employed in DM research, PTFE reflectors are commonly utilized to surround LXe volumes due to their excellent diffuse reflectivity. The critical influence of reflectivity on detector performance, along with the growing interest in assembling thinner PTFE detector walls that maintain high collection efficiency while minimizing light leakages, motivates the need for accurate knowledge of PTFE transmittance (T) and reflectance (R) dependence on PTFE thickness. In this work, a C++/ROOT pulse analysis software is developed to determine T and R at the PTFE–air interface, by using a blue LED light source and PTFE discs of varying thicknesses (from 0.2 ± 0.05 to 5.15 ± 0.05 mm). Measurements are performed at incidence and reflection angles of 30° , 45° and 60° . Attenuation coefficients are consistent across angles ($\lambda_T^{30^\circ} = (1.32 \pm 0.12)$ mm, $\lambda_T^{45^\circ} = (1.33 \pm 0.12)$ mm and $\lambda_T^{60^\circ} = (1.33 \pm 0.13)$ mm), while R shows a strong angular dependence. These results will contribute to the future development of ALPINE detector, whose LXe TPC features a novel PTFE–metal–PTFE interface with light-tight properties yet to be comprehensively characterized.

2 Project details

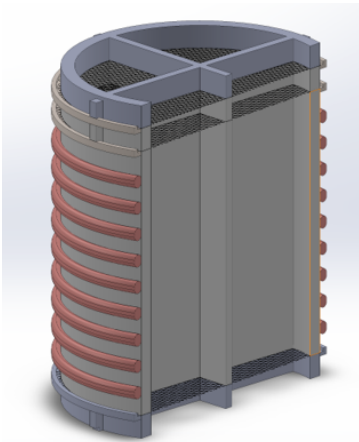
2.1 State-of-the-art and objectives

Observations at astrophysical and cosmological scales indicate that the ordinary visible matter alone is insufficient to describe the entire range of gravitational phenomena characterizing the Universe [1, 2]. This motivated the postulation of Dark Matter (DM), a non-visible form of mass which currently represents the most convincing framework for explaining the observed anomalies of the Universe [3]. The largest class of DM candidates consists of Weakly Interacting Massive Particles (WIMPs), which interact only via gravitational and weak forces [4]. Experiments employing direct detection techniques aim to observe WIMPs scattering off target nuclei, a process which produces measurable signals including the emission of scintillation light resulting from the excitation of target atoms.

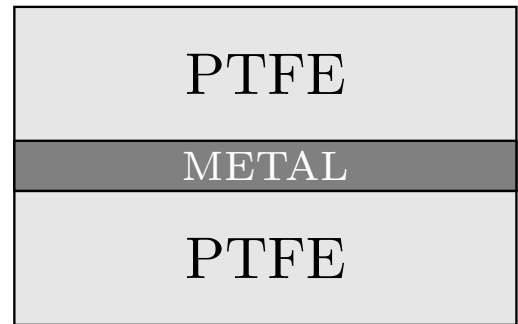
Liquid Xenon (LXe) detectors have proved ideal to reconstruct such scintillation signal, due to their large mass, optical transparency and fiducialization [5–7]. Specifically, LXe scintillation light is centered in the Vacuum Ultra-Violet (VUV) wavelength at ~ 178 nm [8, 9], and its collection efficiency strongly affects LXe detector performances. To maximize light collection efficiency, LXe volumes are enclosed in reflectors made of PTFE (Polytetrafluoroethylene)¹ [10], due to its excellent diffuse reflectivity, being $\sim 99\%$ in the visible and near infrared regions and $\sim 97\%$ in VUV when immersed in LXe [11–13].

Precise knowledge of PTFE reflectance is crucial, as even tiny variations in reflectivity can critically affect sensitivity of LXe detectors. In addition, considerable interest is devoted to the dependence of reflectivity on PTFE thickness, motivated by the desire to reduce material in order to minimize dead volume, outgassing and radioactive background while still ensuring high light collection efficiency [14]. Conversely, a lower limit on PTFE thickness is set by its transmittance properties, as sufficient optical isolation is required to prevent light leakages and losses [15].

The primary objective of this work is to present angle-resolved transmittance (T) and reflectance (R) of PTFE in air as a function of PTFE thickness. These measurements establish the reliability of the employed experimental setup and will contribute to providing reference values for ALPINE LXe detector, which is currently under development for DM research. Particularly, ALPINE segmented TPC (Fig. 1a) features an unexplored PTFE–metal–PTFE interface (Fig. 1b) whose optical properties will enable a deeper understanding of light propagation in the detector volume and will support the optimization of its TPC structure by minimizing photon leakages across the isolated optical regions.



(a) Vertical cross-section of the segmented TPC showing four optically isolated segments and single-piece electrode grids.



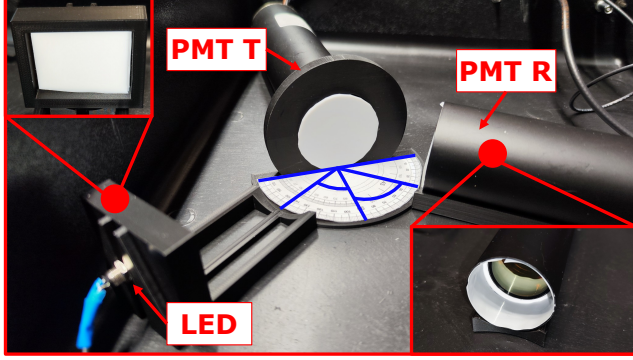
(b) PTFE-metal-PTFE interface to be considered for studying the optical properties of the segmented layers.

Figure 1: Schematic representation of ALPINE detector design and PTFE–metal–PTFE interface.

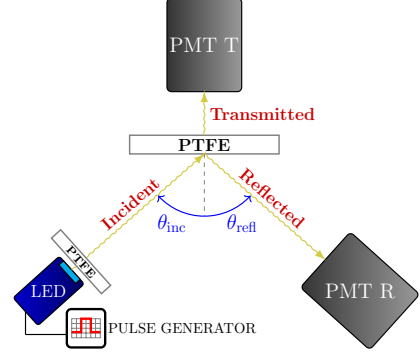
¹PTFE is also known as Teflon, its brand name.

2.2 Methodology

To measure T and R of light at the PTFE–air interface, a blue² LED light source is used. The employed experimental setup, shown in Fig. 2, is located inside a dark box to prevent the intrusion of ambient light. The apparatus consists of the aforementioned blue LED, driven by a pulse generator configured with a frequency of 600 Hz, a high level of 3.5 V, a low level of 2.0 V, 0.0 ns delay, and a pulse width of 70 ns. Three PTFE rectangles of total thickness (4.65 ± 0.05) mm are placed in front of the LED to stabilize its signal in time and to filter out stray light.³ The emitted photons are detected by two HAMAMATSU PMTs, hereafter referred to as PMT T and PMT R, dedicated respectively to T and R measurements. Both PMTs are held firmly in place with 3D-printed holders (displayed in Fig. 2a) and are operated at 1300 V via a high voltage generator. Photon signals from PMTs are recorded using a CAEN digitizer, triggered by the TTL output of the pulse generator.



(a) Photograph of the apparatus.



(b) Schematic diagram of the apparatus.

Figure 2: Employed experimental setup.

Several PTFE discs of three distinct thicknesses (0.20 mm, 1.55 mm, and 2.05 mm) are combined to obtain T and R measurements at eight different effective thicknesses, summarized in Tab. 1. As illustrated in Fig. 2a, these PTFEs are placed in front of PMT T, and are represented schematically by the horizontal PTFE rectangle in Fig. 2b.

Effective thickness [mm]	0.20 mm discs	1.55 mm discs	2.05 mm discs
0.20 ± 0.05	1	0	0
0.80 ± 0.05	4	0	0
1.55 ± 0.05	0	1	0
2.05 ± 0.05	0	0	1
3.10 ± 0.05	0	2	0
3.60 ± 0.05	0	1	1
4.10 ± 0.05	0	0	2
5.15 ± 0.05	0	2	1

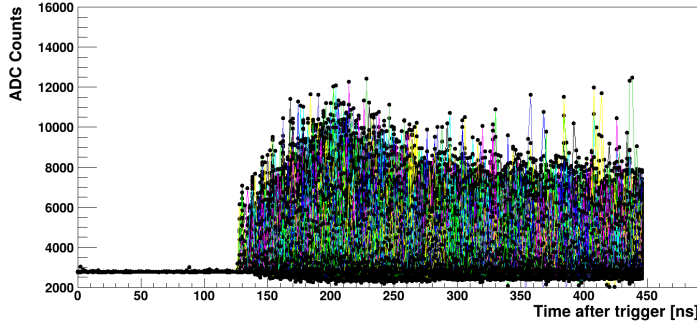
Table 1: Combination of PTFE discs used to achieve different effective thicknesses for T and R measurements.

In addition to investigating T and R dependence on PTFE thickness, the experimental setup in Fig. 2 allows to study their variation with respect to incidence (θ_{inc}) and reflection (θ_{refl}) angles. In particular, measurements were performed at three angular configurations, fixing $\theta_{inc} = \theta_{refl}$ at 30° , 45° and 60° .

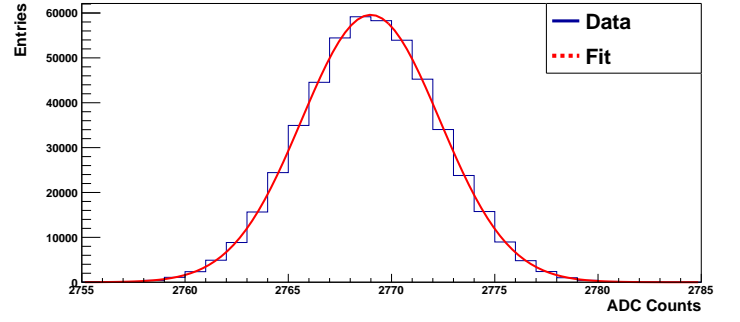
The first step of the analysis is to extract valuable information from the light signals generated by the PMTs. For this purpose, a custom library based on C++ and ROOT is designed (??FAI RELEASE SU GITHUB E CITA LA REPOSITORY??). The digitized signal retrieved from each PMT is illustrated in Fig. 3a. No physical insights can be extrapolated from this plot, except for the waveform baseline and the electronic noise distribution (shown in Fig. 3b), both evaluated in the first 100 ns after the trigger. As indicated in Fig. 3b, a Gaussian fit is performed in order to extract the σ_n for each set of analyzed waveforms.

²Blue light is used as proxy for LXe scintillation light [16].

³Note that the project does not measure T and R of this PTFE, but rather those of the horizontal PTFE shown in Fig. 2b.



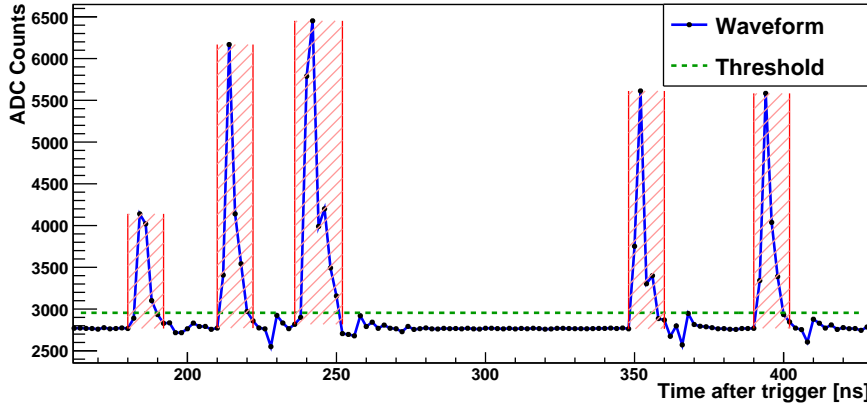
(a) A total of 60 000 raw digitized waveforms is acquired from each PMT, shown here superimposed.



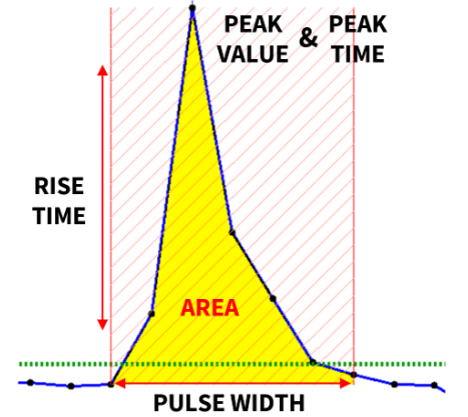
(b) Electronic noise distribution data (blue) and relative fit (red) extracted from the first 100 ns after the trigger.

Figure 3: Superimposed waveforms (expressed in ADC Counts) and corresponding noise characterization, both extrapolated from PMT signals. The trigger, provided by the TTL output of the pulse generator, corresponds to the activation of the blue LED.

Once the value of σ_n is known, it serves as basis for the pulse-finding algorithm. For each waveform, the algorithm search for signal excursions above a threshold t , set as $t = 80 \cdot \sigma_n$. The choice of such a high threshold is justified by the relatively small baseline fluctuations represented by σ_n . To properly account for physical pulses, the waveform signal must not only exceed the threshold value, but also satisfy additional conditions once a candidate pulse maximum is detected. Firstly, the algorithm scans the ADC values around the identified peak to determine the pulse endpoints. Secondly, a minimum separation between consecutive pulses within the same waveform is required to avoid reconstruction artifacts arising from overlapping pulses. After the application of these criteria, valid pulses are identified, as shown in Fig. 4a. Additionally, to validate the correctness of the C++/ROOT software developed for data analysis, key pulse parameters are extracted, including the ones listed in Fig. 4b. For the development of this work, the most significant one is the pulse area A , being proportional to the number of photoelectrons N_{PE} generated by the PMTs. In turn, N_{PE} is proportional to the number of photons detected by the PMTs, N_γ , which is the parameter of interest for T and R .



(a) Physical pulses (blue) within a single waveform, with the threshold (green) used to define them.



(b) Zoomed-in view of a single pulse with some of its relevant parameters.

Figure 4: Illustration of physical pulses and their parameters.

To compute the pulse area, PMT signals are integrated using the following discrete sum over the pulse width:

$$A = \sum_{\text{pulse width}} \left(V_i^{\text{ADC}} - V_{\text{baseline}}^{\text{ADC}} \right) \Delta t, \quad (1)$$

where V_i^{ADC} and $V_{\text{baseline}}^{\text{ADC}}$ are respectively the ADC values of the i -th sample and of the baseline and Δt is the sampling interval (2.0 ns for the employed digitizer). Using Eq. 1, it is possible to plot the distribution of pulse areas as a function of the time after trigger, shown in Fig. 5a. To calibrate the signal scale and to check that our experimental setup reliably detects single and possibly multiple photon events, the area in Fig. 5a is converted into the number of photoelectrons (PE), as illustrated in Fig. 5b. In the latter, two distinct peak centered around 1 and 2 PE are clearly visible, which correspond to the single- and double-PE events, respectively. Each PE peak in Fig. 5b is well described by a two-sided Gaussian fit, illustrated in the same plot.

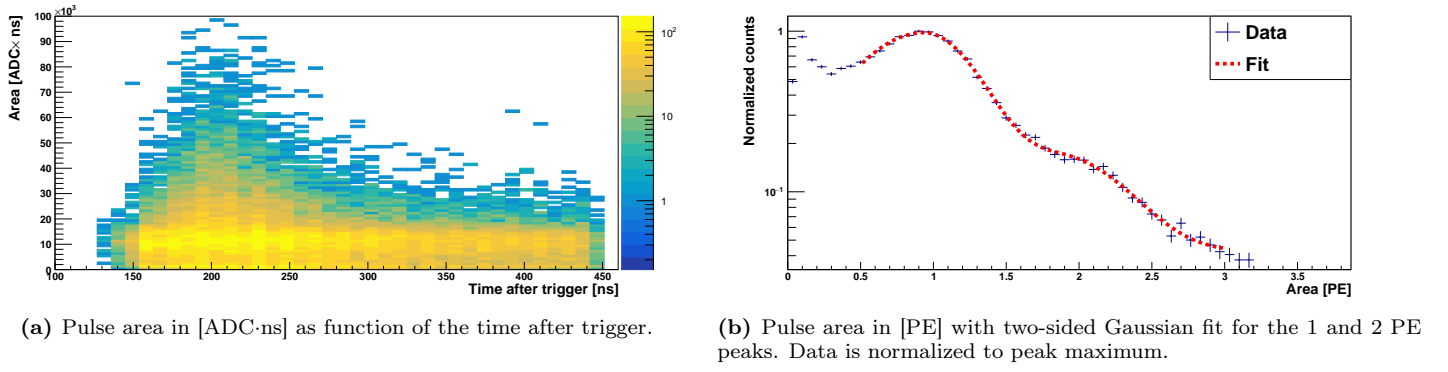
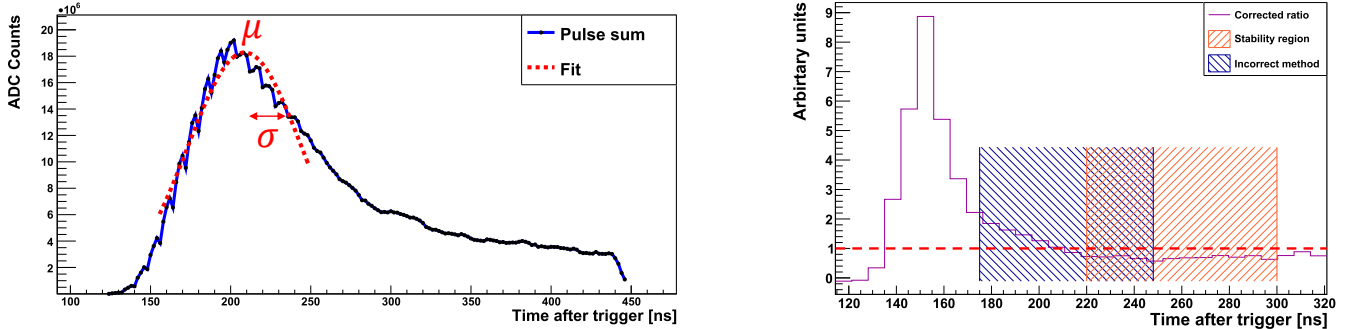


Figure 5: Pulse area distributions plotted using different unit of measurements.

The next step of the analysis is to divide waveforms into temporal regions relative to the trigger: a pre-integration region (containing baseline pulses), an integration region (where physical pulse areas are summed to compute the total collected light), and two post-integration regions (containing delayed pulses). To define the integration region, all pulses from Fig. 3a are summed to obtain the distribution in Fig. 6a, which is then fitted with a Gaussian function to extrapolate mean (μ) and width (σ). A first approach determines the integration window as the interval $[\mu - \sigma, \mu + \sigma]$; however, this method introduces a bias. This is evident by introducing the histogram $H(t)$:

$$H(t) = \frac{S_R(t)}{S_T(t)}, \quad (2)$$

where $S_R(t)$ and $S_T(t)$ are respectively the pulse sum distributions of reflected⁴ and incident photons.⁵ Ideally, since $H(t)$ would represent a instantaneous ratio of R ,⁶ it should be constant in time, as no component in our experimental setup would cause R to change in time. However, by plotting $H(t)$ in Fig. 6b, time-dependent variations can be seen, probably introduced by different time responses of PMT T and PMT R. Thus, as illustrated in Fig. 6b, the window of the first approach (in blue) is not optimal, as it lies within an unstable range of $H(t)$. Conversely, a more reliable integration interval is chosen where $H(t)$ is stable (in orange), specifically within [220, 300] ns.



(a) Pulse sum graph obtained by summing all the pulses extracted from the superimposed waveform plot in Fig. 3a.

(b) $H(t)$ (purple) defined as indicated in Eq. 2. The blue region represents the integral window defined with the first, incorrect approach, while the orange region, falling within [220, 300] ns, corresponds to the chosen, unbiased integration region.

Figure 6: Plots used to define the integration region.

T and R are defined through the average PE rate r , computed summing pulse areas over the integration region shown in Fig. 6b:

$$r = \frac{\sum_{int} (\text{Pulse area})}{\Delta t_{int} \cdot N_{waveforms}}, \quad (3)$$

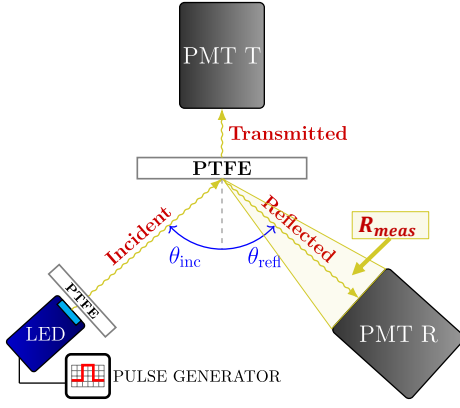
where $\Delta t = 80$ ns and $N_{waveforms} = 60\,000$ are the time duration and the number of the analyzed waveforms, respectively. Using Eq. 3, T and R are finally obtained as follows:

$$T = \frac{r^{tran}}{r^{inc}} \quad \text{and} \quad R = \frac{r^{refl} - r^{direct}}{r^{inc}}. \quad (4)$$

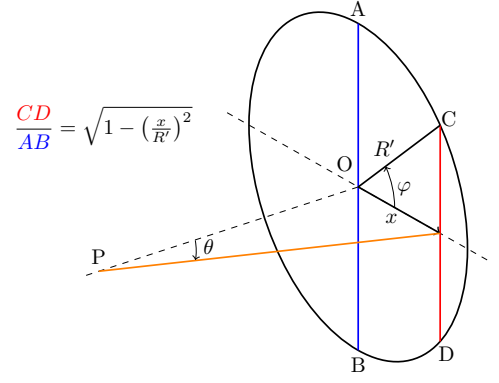
⁴Reflected photons are measured with PMT R after subtracting the photons traveling directly from the LED to PMT R. Direct photon contribution is particularly relevant at large θ_{inc} and θ_{refl} , as can be viewed from Fig. 2.

⁵Incident photons are measured with PMT T by removing the horizontal PTFE layer in Fig. 2b.

⁶Note that $H(t)$ is merely used as sanity check to define an unbiased integration region. It does not represent the physical reflectance.



(a) Experimental setup with highlighted solid angle subtended by PMT R, within which R_{meas} is defined.



(b) Scheme illustrating the non-uniformity of light acceptance and the chord-diameter ratio.

Figure 7: Scheme of the geometric acceptance corrections applied to R .

In contrast to T , R needs to be corrected to account for the geometric acceptance of PMT R. Specifically, measured reflectance R_{meas} is underestimated due to the limited solid angle subtended by PMT R's acceptance window, illustrated in Fig. 7a. To account for the absolute reflectance R_{true} , a geometrical correction factor f_{acc} is introduced, such that $R_{true} \approx f_{acc} \cdot R_{meas}$. f_{acc} is specified in Eq. 5 employing the reflectivity function F defined in [17], which models the specular and diffusive components of PTFE reflection:

$$f_{acc} = \frac{\int_{\theta_{min}}^{\theta_{max}} F(\theta_{refl}) d\theta_{refl}}{\int_{-90^\circ}^{90^\circ} F(\theta_{refl}) d\theta_{refl}} \quad \text{with} \quad F(\theta_{inc}, \theta_{refl}) = R_1(\theta_{inc}) e^{-\frac{\alpha^2(\theta_{inc}, \theta_{refl})}{2\sigma^2}} + R_2(\theta_{inc}) \cos(\theta_{refl}), \quad (5)$$

where $[\theta_{min}, \theta_{max}]$ are the endpoints of PMT R's acceptance window. Furthermore, since PMT R's aperture is circular (Fig. 2a), acceptance is not uniform across θ_{refl} , as can be seen in Fig. 7b. Consequently, photons at larger angles hit the circular aperture with lower probabilities. To take into account the circular hole correction, f_{acc} 's numerator is weighted with the chord-diameter ratio defined in Fig. 7b. Both geometrical corrections are finally accounted by f'_{acc} :

$$f'_{acc} = \frac{\int_{\theta_{min}}^{\theta_{max}} F(\theta_{refl}) \sqrt{1 - \left(\frac{\theta_{refl} - \theta_{inc}}{R'}\right)^2} d\theta_{refl}}{\int_{-90^\circ}^{90^\circ} F(\theta_{refl}) d\theta_{refl}}, \quad (6)$$

where $R' = 25^\circ$ denotes the angular radius of PMT R. In the following, absolute R values, defined as $R_{true} \approx R_{meas}/f'_{acc}$, will be considered.

2.3 Results

Measurements of T and R at the different PTFE thicknesses listed in Tab. 1 are summarized in Tab. 2, with data divided by incidence and reflection angles $\theta_{inc} = \theta_{refl} = 30^\circ, 45^\circ$ and 60° . The corresponding dependencies of T and R on both thickness and angular configurations are illustrated in Fig. 8a, Fig. 8b and Fig. 8c. As expected from [18], T decreases with thickness for all angles, and its values show compatibility with previous measurements [19]. Moreover, by fitting T data with a Beer-Lambert law $T = Ae^{-x/\lambda_T} + B$, it is possible to extrapolate the attenuation coefficient λ_T . As outlined in Fig. 8, λ_T is consistent among the three angular configurations.

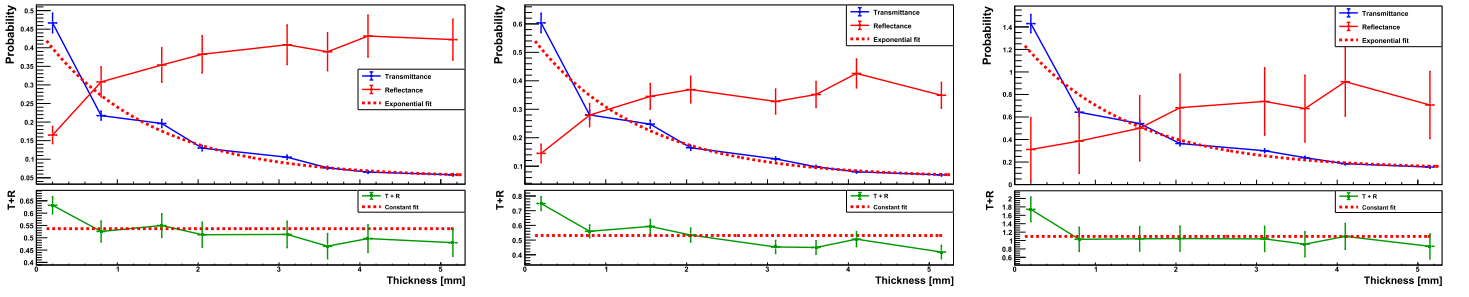
Contrary to T , R data shows an increasing trend with thickness for all three configurations. While higher reflectivity values are obtained for 60° at larger PTFE thicknesses, R does not reach the expected order of magnitude reported in Sec. 2.1, which may be attributed to the lack of surface finish on the employed PTFE discs. Additionally, R measurements are not fully compatible across $30^\circ, 45^\circ$ and 60° , confirming their strong dependence on observation angles [20].

In addition to T and R , Fig. 8a, Fig. 8b, and Fig. 8c also report the sum $T + R$, evaluated with a constant fit to verify the efficiency.⁷ The fits exhibit a slight decreasing trend with thickness across all configurations, suggesting possible absorption. Moreover, the constant fits at 30° and 45° are not compatible with the 60° configuration, indicating that the different angles do not share the same efficiency.

Thickness [mm]	30°		45°		60°	
	T	R	T	R	T	R
0.20 ± 0.05	0.467 ± 0.026	0.165 ± 0.023	0.604 ± 0.034	0.145 ± 0.032	1.429 ± 0.081	0.311 ± 0.283
0.80 ± 0.05	0.217 ± 0.012	0.308 ± 0.041	0.280 ± 0.016	0.280 ± 0.041	0.642 ± 0.036	0.386 ± 0.286
1.55 ± 0.05	0.196 ± 0.011	0.354 ± 0.046	0.248 ± 0.014	0.345 ± 0.045	0.541 ± 0.031	0.500 ± 0.290
2.05 ± 0.05	0.130 ± 0.007	0.382 ± 0.050	0.165 ± 0.009	0.369 ± 0.047	0.364 ± 0.021	0.683 ± 0.297
3.10 ± 0.05	0.105 ± 0.006	0.408 ± 0.053	0.126 ± 0.007	0.327 ± 0.044	0.301 ± 0.017	0.738 ± 0.299
3.60 ± 0.05	0.077 ± 0.004	0.389 ± 0.051	0.098 ± 0.006	0.352 ± 0.046	0.239 ± 0.014	0.675 ± 0.297
4.10 ± 0.05	0.065 ± 0.004	0.431 ± 0.056	0.080 ± 0.005	0.426 ± 0.051	0.185 ± 0.010	0.306 ± 0.306
5.15 ± 0.05	0.058 ± 0.003	0.422 ± 0.055	0.069 ± 0.004	0.349 ± 0.045	0.155 ± 0.009	0.706 ± 0.298

Table 2: T and R values for different PTFE thicknesses and angular configurations.

⁷That is, whether T and R add up to unity.



(a) $\theta_{\text{inc}} = \theta_{\text{refl}} = 30^\circ$. Fitted attenuation coefficient and constant $T + R$ yield respectively $\lambda_T^{30^\circ} = (1.32 \pm 0.12)$ mm and 0.537 ± 0.017 .

(b) $\theta_{\text{inc}} = \theta_{\text{refl}} = 45^\circ$. Fitted attenuation coefficient and constant $T + R$ yield respectively $\lambda_T^{45^\circ} = (1.33 \pm 0.12)$ mm and 0.531 ± 0.016 .

(c) $\theta_{\text{inc}} = \theta_{\text{refl}} = 60^\circ$. Fitted attenuation coefficient and constant $T + R$ yield respectively $\lambda_T^{60^\circ} = (1.33 \pm 0.13)$ mm and 1.10 ± 0.10 .

Figure 8: T and R plots for different PTFE thicknesses and angular configurations. Top: T and R with Beer-Lambert law fits. Bottom: $T + R$ sum with constant fits.

To conclude, further studies are required to account for systematic uncertainties that strongly affect reflectance, such as PTFE density, temperature, surface finish, manufacturing process and purity [21]. Finally, the reproduced T and R at PTFE–air interface will be employed to test the PTFE–metal–PTFE for optimizing ALPINE detector and the light tightness of its segmented TPC.

2.4 Your contributions as a S3P3 student

My personal contributions to the project include the development of the C++/ROOT analysis software employed for pulse finding and integration (Fig. 3, Fig. 4 and Fig. 6), the calibration of PMT T and PMT R single- and double- PE peaks (Fig. 5), the data acquisition for all PTFE sample thicknesses and the final analysis of T and R (Fig. 8), including the application of the geometric acceptance corrections (Fig. 7).

References

- [1] V. C. Rubin, W. K. Ford Jr., and N. Thonnard. “Extended rotation curves of high-luminosity spiral galaxies. IV. Systematic dynamical properties, Sa through Sc”. *Astrophys. J. Lett.* 225 (1978), pp. L107–L111.
- [2] P. A. R. Ade et al. “Planck2013 results. I. Overview of products and scientific results”. *Astronomy and Astrophysics* 571 (Oct. 2014), A1.
- [3] T. M. Undagoitia and L. Rauch. “Dark matter direct-detection experiments”. *Journal of Physics G: Nuclear and Particle Physics* 43.1 (Dec. 2015), p. 013001.
- [4] K. GRIEST. “The Search for the Dark Matter: WIMPs and MACHOs”. *Annals of the New York Academy of Sciences* 688.1 (June 1993), 390–407.
- [5] J. Angle et al. “First Results from the XENON10 Dark Matter Experiment at the Gran Sasso National Laboratory”. *Physical Review Letters* 100.2 (Jan. 2008).
- [6] V. N. Lebedenko et al. “Results from the first science run of the ZEPLIN-III dark matter search experiment”. *Physical Review D* 80.5 (Sept. 2009).
- [7] D. Akerib et al. “Results from a Search for Dark Matter in the Complete LUX Exposure”. *Physical Review Letters* 118.2 (Jan. 2017).
- [8] J. Jortner et al. “Localized Excitations in Condensed Ne, Ar, Kr, and Xe”. *The Journal of Chemical Physics* 42.12 (June 1965), pp. 4250–4253.
- [9] N. Basov et al. “Luminescence of condensed Xe, Kr, Ar and their mixtures in vacuum region of spectrum under excitation by fast electrons”. *Journal of Luminescence* 1-2 (1970), pp. 834–841.
- [10] T. L. Collaboration et al. “LUX-ZEPLIN (LZ) Conceptual Design Report”. 2015.
- [11] V. Weidner and J. Hsia. “Reflection properties of pressed polytetrafluoroethylene powder”. *Journal of the Optical Society of America* 71 (July 1981), pp. 856–861.
- [12] D. Akerib et al. “The Large Underground Xenon (LUX) experiment”. *Nuclear Instruments and Methods in Physics Research Section A: Accelerators, Spectrometers, Detectors and Associated Equipment* 704 (Mar. 2013), pp. 111–126.
- [13] F. Neves et al. “Measurement of the absolute reflectance of polytetrafluoroethylene (PTFE) immersed in liquid xenon”. *Journal of Instrumentation* 12.01 (Jan. 2017), P01017–P01017.
- [14] E. Aprile et al. “Material radioassay and selection for the XENON1T dark matter experiment”. *The European Physical Journal C* 77.12 (Dec. 2017).
- [15] J. Haefner et al. “Reflectance dependence of polytetrafluoroethylene on thickness for xenon scintillation light”. *Nuclear Instruments and Methods in Physics Research Section A: Accelerators, Spectrometers, Detectors and Associated Equipment* 856 (June 2017), pp. 86–91.
- [16] S. Ghosh et al. “Dependence of polytetrafluoroethylene reflectance on thickness at visible and ultraviolet wavelengths in air”. *Journal of Instrumentation* 15.11 (Nov. 2020), P11031–P11031.
- [17] C. Levy. “Light Propagation and Reflection off Teflon in Liquid Xenon Detectors for the XENON100 and XENON1T Dark Matter Experiment”. PhD thesis. U. Munster, 2014.
- [18] D. Cichon et al. “Transmission of xenon scintillation light through PTFE”. *Journal of Instrumentation* 15.09 (Sept. 2020), P09010–P09010.
- [19] B. Tsai et al. “A Comparison of Optical Properties between High Density and Low Density Sintered PTFE”. *Proceedings of SPIE - The International Society for Optical Engineering* 7065 (Aug. 2008).
- [20] P. Barnes, A. Parr, and E. Early. “Spectral Reflectance”. en. 1998.
- [21] C. F. P. d. Silva. “Study of the Reflectance Distributions of Fluoropolymers and Other Rough Surfaces with Interest to Scintillation Detectors”. PhD Thesis. Universidade de Coimbra, 2009.